15.6 COMPARING AEROSOL AND LOW-LEVEL MOISTURE INFLUENCES ON SUPERCELL TORNADOGENESIS: IDEALIZED SIMULATIONS

David G. Lerach and William R. Cotton
Colorado State University, Fort Collins, Colorado

1. Introduction

Aerosols, both natural and anthropogenic, can impact hydrometeor formation, cloud processes, and precipitation by acting as cloud condensation nuclei (CCN). An enhancement in CCN concentrations tends to increase resulting cloud droplet concentrations that are of smaller sizes than would have otherwise formed. This creates more narrow cloud droplet spectra and reduced collision efficiencies, thus inhibiting the warm-rain process (Hobbs et al. 1970; Eagan et al. 1974; Braham et al. 1981; Kaufman and Nakajima 1993; Rosenfeld 1999, 2000). Studies by Seifert and Beheng (2006) and van den Heever et al. (2006) showed that in deep convection, higher CCN concentrations can lead to more supercooled water aloft, which creates stronger mature updrafts aloft via enhanced latent heating effects. Being that hailstone growth principally occurs in the updraft where there is a close match between updraft velocities and the fall velocities of the stones (Foote 1984), enhanced aerosol concentrations acting as CCN could possibly aide in the production of larger hail in convective storms. Regarding supercell thunderstorms, Weisman and Bluestein (1985) were among the first to suggest the importance of microphysical parameters to supercell dynamics. van den Heever and Cotton (2004) and Gilmore et al. (2004) performed idealized numerical simulations, finding that increasing the mean diameter of rain and hail distributions (all else being equal) reduced evaporative cooling and melting rates, which produced weaker low-level downdrafts and weaker, shallower cold-pools. Likewise, simulations by Storer et al. (2010) found that enhancing CCN concentrations in supercell storms led to a reduction in the warm rain process, producing fewer but larger raindrops. This also reduced evaporative cooling within downdraft regions and produced weaker, shallower cold-pools. The increased CCN concentrations also resulted in a decrease in net accumulated precipitation. These general results suggest a possible link between aerosols and supercell tornadogenesis.

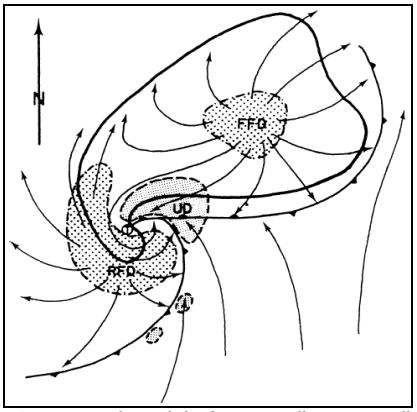

Fig. 1: Conceptual model of a tornadic supercell at the surface. The location most favorable for tornado formation is identified by an encircled T. [From Lemon and Doswell (1979).]

Figure 1 depicts the structure of a tornadic supercell as described by Lemon and Doswell (1979). The main components include the main updraft (UP), forward flank downdraft (FFD), rear flank downdraft (RFD), and associated gust fronts. While the precise mechanisms of supercell tornadogenesis remain unknown, multiple studies suggest that these tornadoes are often linked to the RFD, which can transport vertical vorticity to the surface, baroclinically generate horizontal vorticity, and enhance convergence along gust fronts beneath the updraft (Burgess et al. 1977; Davies-Jones 1982a,b; Davies-Jones and Brooks 1993; Walko 1993; Brooks et al. 1994; Wicker and Wilhelmson 1995; Trapp and Fiedler 1995; Markowski 2002).

Ludlam (1963) first argued that tornadogenesis is more likely to occur when the temperature deficit within the RFD is

* Corresponding author address: David G. Lerach, Colorado State University, Dept. of Atmospheric Science, Fort Collins, CO 80523; email: dlerach@atmos.colostate.edu

small relative to the environment. The theory was later supported by observations (Lemon 1974; Nelson 1977; Brandes 1978) and idealized numerical simulations (Eskridge and Das 1976; Davies-Jones 2000; Leslie and Smith 1978). Observational and numerical modeling studies by Markowski et al. (2002, 2003), utilizing VORTEX data, found that air parcels within RFDs tended to be less negatively buoyant and thus warmer in tornadic vs. nontornadic supercells. Tornadic vortices increased in intensity and longevity as downdraft parcel buoyancy increased, because colder parcels were more resistant to lifting. Snook and Xue (2008) extended the work of van den Heever and Cotton (2004) and Gilmore et al. (2004) to tornadogenesis, verifying that larger raindrops and hailstones yielded warmer cold-pools via reduced evaporative cooling. In addition, the larger hydrometeors, with greater terminal fallspeeds, were not advected as far from the updraft before falling to the ground, reducing the areal coverage of precipitation. This positioned the gust front closer to the storm center, permitting vertically oriented updrafts and vertical alignment of low- and mid-level vertical vorticity. This in turn increased the dynamic suction effect by the mesocyclone (Rotunno and Klemp 1982) and associated low-level vertical stretching, thereby increasing the potential for tornadogenesis.

Lerach et al. (2008) assessed possible aerosol indirect microphysical effects on supercell tornadogenesis using idealized simulations. Enhanced CCN and GCCN concentrations reduced warm- and cold-rain processes within the RFD and FFD, resulting in lower precipitation rates. A relatively weak cold-pool was produced at the updraft-downdraft interface due to lower evaporative cooling rates, providing a favorable environment for tornadogenesis, where the low-level mesocyclone and near-surface vorticity provided by the RFD-based gust front remained vertically-stacked. This resulted in the formation of an EF-1 tornado while the case with lower aerosol concentrations failed to produce such a vortex. Heavier precipitation in the RFD and FFD in the clean simulation produced more evaporative cooling, and thus a stronger surface cold-pool that surged and destroyed the RFD structure. This resulted in a single gust front that advected away more rapidly from the storm system, separating the low-level vorticity source from the parent storm and thus hindering tornadogenesis. Studies such as Weisman and Klemp (1982) and Brooks et al. (1994) found similar potential failure mechanisms.

While the results of Lerach et al. (2008) provided insight to the possible role of aerosols in influencing supercell storms and tornadogenesis, the relative impact must be put into context with other environmental parameters, particularly convective available potential energy (CAPE) and low-level moisture. VORTEX observations have shown that tornado likelihood, intensity, and longevity increase as the CAPE (potential buoyancy) within the RFD increases (Markowski et al. 2002). In addition, observations and idealized model simulations by Markowski et al. (2002, 2003) found that higher relative humidity at low levels was more conducive to RFDs associated with relatively high buoyancy and higher tornadogenesis potential. However, Markowski et al. (2003) note that less idealized, three-dimensional numerical studies with sophisticated microphysics and relatively fine-scale horizontal grid spacing (~100 m) should be performed and compared with their results. Therefore, the goal of this study is to compare the role of aerosol indirect microphysics with that of low-level moisture and CAPE on supercell tornadogenesis using a sophisticated mesoscale model with inner grid spacing on the order of 100 m. We perform an ensemble of numerical simulations of an idealized supercell thunderstorm, differing only in initial background CCN concentrations and environmental low-level moisture. The simulations are compared to assess which scenarios are most favorable for tornadogenesis. While the definition of a numerically-simulated tornado remains somewhat subjective, this study defines a simulated tornado as a low-level vortex that meets the following criteria, slightly modified from Wicker and Wilhelmson (1995): (i) The vortex forms in conjunction with a supercell mesocyclone (ii) The vortex is characterized by highly convergent swirling winds affecting a relatively narrow path, and (iii) The near-surface winds exceed minimum EF-1 intensity (~39 m s^{-1}).

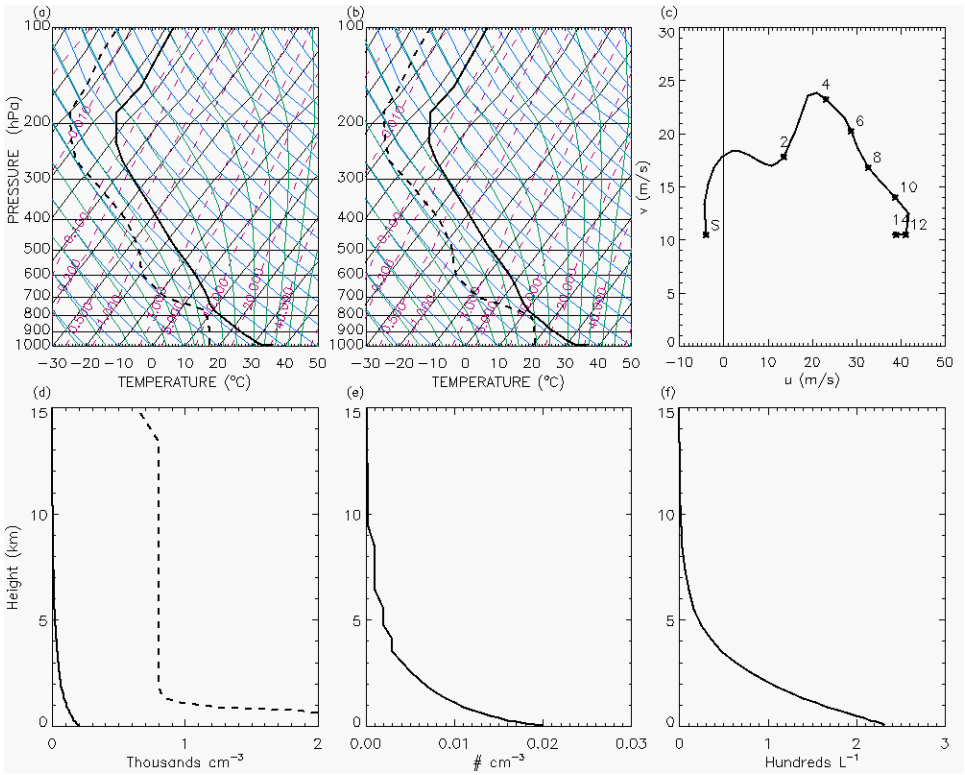

Fig. 2: Initial background profiles of (a) temperature and dew point temperature for the low-moisture simulations, (b) temperature and dew point temperature for the high-moisture simulations, (c) horizontal wind represented by a hodograph, (d) CCN, (e) GCCN, and (f) IN concentrations. Note that in Fig. 2c, 'S' represents the surface wind vector and vectors are labeled every 2 km. In Fig. 2d, the solid and dashed curves represent the "clean continental" and dusty/polluted CCN profiles, respectively.

2. Model Setup

This study utilized the Regional Atmospheric Modeling System (RAMS; Pielke et al. 1992) version 4.3.0 (Cotton et al. 2003) in a Cartesian coordinate domain. RAMS makes use of the non-hydrostatic/compressible forms of the basic model equations (Tripoli and Cotton 1986). The model uses a staggered Arakawa-C grid (Arakawa and Lamb 1981) with terrain-following sigma coordinates in the vertical (Tripoli and Cotton 1980). Time differencing is performed via a hybrid combination, with the calculation of the Exner function done with a leapfrog scheme and all other variables with a forward scheme. The grid domain included three two-way interactive nested model grids (Clark and Farley 1984) with horizontal grid spacing of 1000, 333.33, and 111.11 m respectively. The outer-most grid (Grid 1), used for generating convection, had horizontal dimensions of 149x149 km. Grid 2, centered over Grid 1 coordinates (74.2 km, 54.2 km), had dimensions of 60.33x60.33 km and was used to simulate the scale of the supercell environment. Grid 3 was centered over Grid 2 coordinates (23.9 km, 35.6 km) and had horizontal dimensions of 38.44x21.78 km. This inner grid was used to assess the evolution of the mesocyclone and any tornado-like vortices. Grids 1, 2, and 3 had time steps of 3, 1, and 0.333 s, respectively. Each grid contained 39 vertical grid levels with spacing increasing from 50 m near the ground to a maximum of 1 km.

A bin-emulating, two-moment bulk microphysics scheme (Saleeby and Cotton 2008) was utilized in these simulations, which included a microphysical category of large cloud droplets (cloud2) to better represent the frequently bimodal distribution of cloud droplet spectra. The scheme explicitly predicted mixing ratios and number concentrations of pristine ice, snow, aggregates, graupel, hail, cloud and cloud2 droplets, and rain. Nucleation by CCN, GCCN, and ice nuclei (IN) were explicitly considered. CCN directly nucleated to form cloud droplets, while GCCN directly nucleated to form cloud2 droplets. We in

Table 1: Experiment names and parameters. CCN concentrations (cm^{-3}) and mixing ratios ($g\ kg^{-1}$) represent values at the surface.

Experiment	CCN	Water Vapor Mixing Ratio
CLN1	200	12.6
CLN2	200	15.75
DST1	2000	12.6
DST2	2000	15.75

the model excluded the effects of terrain, surface fluxes, surface drag, radiation, and friction due to the time scales involved and the desire to simplify the experiment. Convection was explicitly resolved on all grids. Surface vegetation was assumed to be composed of crop/mixed farming, and the soil type was prescribed as sandy clay loam.

The initial soundings and vertical wind profile utilized were adapted from a previously employed setup that was found to generate storm-splitting and supercells (Grasso 2000; van den Heever and Cotton 2004; Gaudet and Cotton 2006; Lerach et al. 2008). This study focused on the right-moving storms. Convection was initiated by introducing a "warm, moist bubble" (10x10x1.5 km, 3 K thermal perturbation, 20% moisture perturbation) at the surface. The model aerosol species were set initially horizontally homogeneous with prescribed vertical profiles of CCN, GCCN, and IN concentrations. In all, four simulations were performed. In two simulations, the initial background CCN concentrations were set to represent a relatively "clean continental" environment. In the other two simulations, CCN concentrations were increased to represent an aerosol-rich environment due to the presence of dust (Koehler et al. 2009) or other pollutants. The background water vapor mixing ratios below 800 mb differed by 20% for each pair of CCN simulations. Figure 2 displays the initial profiles of temperature and dew point temperature (Fig. 2a-b), horizontal wind (Fig. 2c), CCN (Fig. 2d), GCCN (Fig. 2e), and IN (Fig. 2f). Due to the tendency of convection to propagate off of Grid 1, a constant mean storm motion vector of u = 14.1 m s^{-1}, v = 14.1 m s^{-1} was subtracted from the hodograph (Fig. 2c) at the time of initialization. Table 1 summarizes the differences between the four simulations conducted. The simulation with "clean continental" background CCN and relatively low (high) relative humidity below 800 mb will be referred to as the CLN1 (CLN2) simulation. The simulation with dusty, or polluted, background CCN and relatively low (high) relative humidity below 800 mb will be referred to as the DST1 (DST2) simulation. CCN concentrations near the surface were set to 200 cm^{-3} and 2000 cm^{-3} for the CLN and DST simulations, respectively (Fig. 2d), based on CRYSTAL-FACE measurements (van den Heever et al. 2006). While GCCN and IN concentrations are thought to be important to convective processes, their effects are not addressed at this time. The background initial profiles of GCCN (Fig. 2e) and IN (Fig. 2f) were held fixed for all four simulations. Simulations lasted 110 min. Grid 2 was initialized at 40 min. Grid 3 was initialized at 60 min.

3. Results

a. Storm evolution

The development of the convection closely resembles that of other modeled supercells in the literature (Klemp and Wilhelmson 1978a,b; Wilhelmson and Klemp 1981; Ray et al. 1981; Grasso and Cotton 1995; Gaudet and Cotton 2006; Lerach et al. 2008). Each simulation produces storm splitting, and both a right moving, cyclonically rotating supercell and left moving, anticyclonically rotating supercell are evident at 55 min (not shown). The left mover moves out of the grid domain and is not considered further. Figure 3 displays simulated reflectivity at 1 km above ground level (hereafter, all heights AGL) on Grid 2 for all four simulations in 15-min increments from 65-110 min simulation time. Updrafts (downdrafts) greater than 10 (5) m s^{-1} at 3.5 km are overlaid. For simplicity the positive "y," negative "y," positive "x," and negative "x" directions will be referred to as north, south, east, and west, respectively. By 65 min, the simulated right movers possess well-defined hooks in the reflectivity, associated with the RFD precipitation wrapping around the main updraft. The storms initialized with higher moisture values below 800 mb (hereafter, HM) are greater in horizontal extent compared to the storms initialized with lower moisture values (hereafter, LM), shown in Fig. 3 as larger regions of reflectivity greater than 0 dBZ. In particular, the 40+ dBZ cores associated with the RFD and FFD

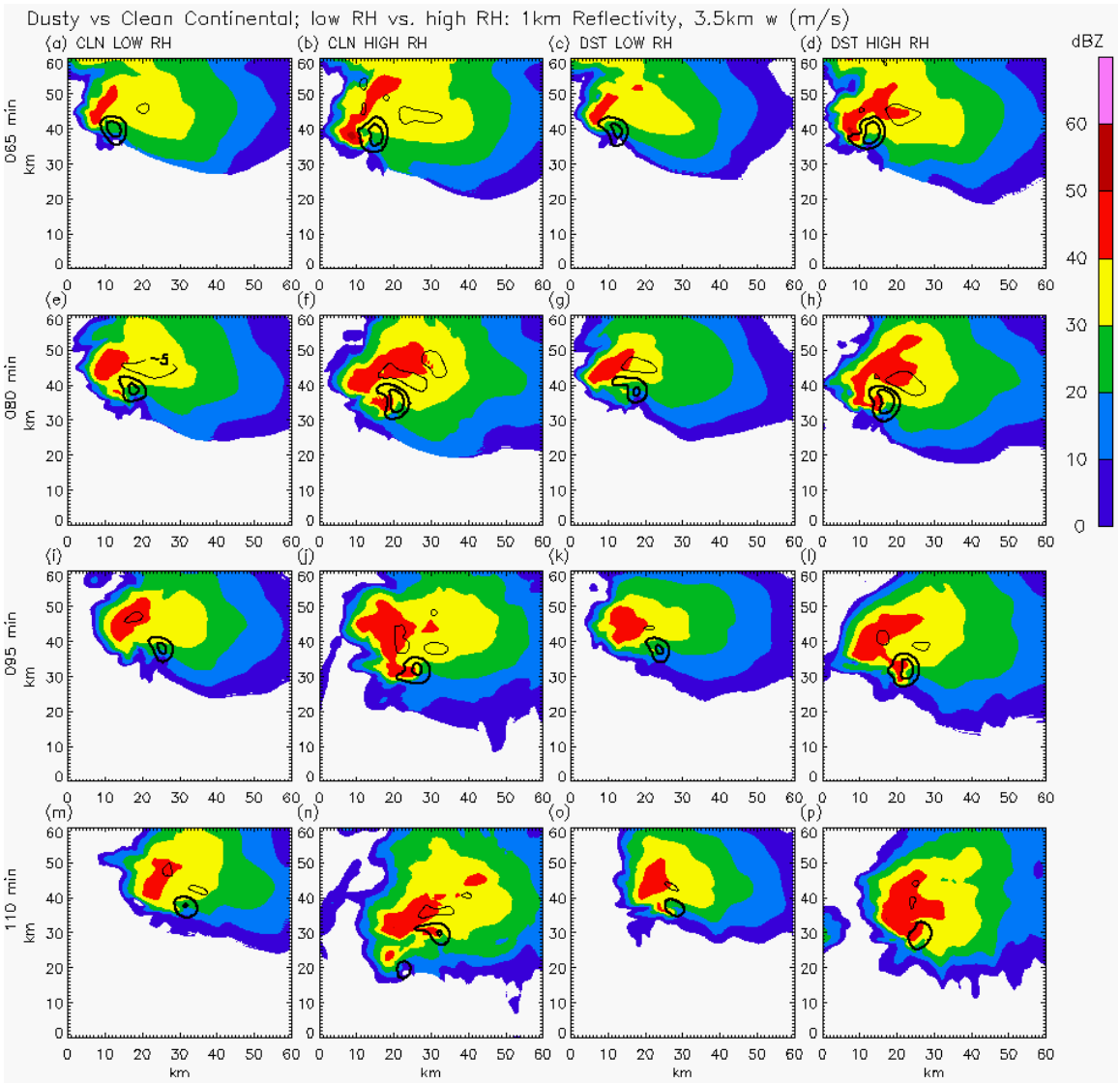

Fig. 3: Simulated 1-km reflectivity on Grid 2 at 65, 80, 95, and 110 min (rows 1-4, respectively) for the CLN1, CLN2, DST1, and DST2 (columns 1-4, respectively) simulations. Vertical velocities of –5, 10, and 20 m s^{-1} at 3.5 km are overlaid with thick (thin) contours for updrafts (downdrafts).

precipitation are noticeably larger in the HM cases throughout the simulated time span. Therefore, the cyclonically curved reflectivity hook associated with the RFD is more pronounced in the HM cases. This is all to be expected, as the HM simulations were initialized with 20% more available moisture below 800 mb, and therefore initialized with 59% higher CAPE (3517 vs. 2207 J kg^{-1}), suggesting more intense convection and precipitation in the HM simulations. This coincides with the fact that the HM supercells possess larger updraft and downdraft cores at 3.5 km compared to the LM cases. It also appears that the clean continental storms contain larger regions of significant downdrafts compared to the dusty storms, most noticeable after 65 min. Profiles of mean and maximum vertical motion within both updraft and downdraft regions were constructed at five-minute intervals for all four simulations on Grid 2 (not shown). They suggested that the HM simulations produced stronger peak updrafts than the LM storms, and the CLN2 simulation often produced slightly stronger updrafts than the DST2 simulation. The HM simulations also produced stronger low-level (below 5 km) downdrafts compared to the LM simulations, on average. The DST1 storm produced the weakest overall downdrafts. The CLN2 simulation produced

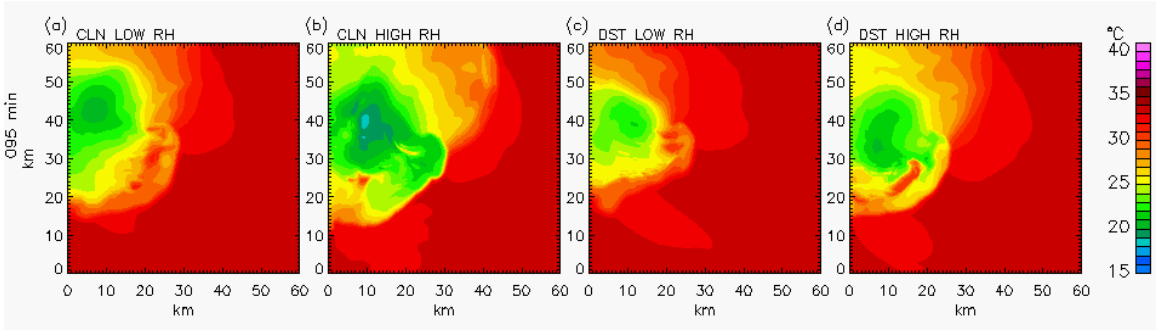

Fig. 4: Same as Fig. 3i-l but for near-surface (24 m) temperature on Grid 2 at 95 min.

the strongest downdrafts through 80 min. However, from 85 min on the CLN1 supercell yielded the strongest downdrafts at low levels. The DST2 simulation generally produced stronger downdrafts than the DST1 storm throughout the simulated time period. These results coincide with the general differences seen in cold-pool evolution between simulations. Notice that the FFD regions in all four simulations grow in horizontal extent with time through 95 min, seen in the reflectivity fields by the 40+ dBZ contours (Fig. 3). Figure 4 displays near-surface (24 m) temperature on Grid 2 for all simulations at 95 min. It is clear that both low-level moisture and CCN concentration played contributing roles to the size and strength of the resulting cold-pools. The CLN2 supercell produces the largest and strongest cold-pool, with minimum temperatures reaching 18°C and a significant region reaching 21°C. The DST1 supercell produces the smallest and weakest cold-pool, with minimum temperature values only reaching 21°C over an approximate 2x2 km region. The CLN1 and DST2 supercells produce comparable cold-pools, with minimum temperatures around 20°C. However, the CLN1 region of 20°C air covers an area of roughly 6x6 km, while that of the DST2 simulation spans an area of roughly 4x4 km. Additionally, the minimum cold-pool temperatures are located back in the FFD region in the CLN1 simulation, while minimum cold-pool temperatures in the DST2 simulation are located closer to the RFD and leading storm outflow. Notice that the CLN2 supercell has the strongest horizontal temperature gradient across the RFD-based gust front, but the DST2 supercell produces the second strongest gradient. By 110 min the LM storms continue to exhibit a "classical" supercellular structure, while the HM storms become less organized (Fig. 3) and begin to exhibit some high-precipitation (HP)-like characteristics. The CLN2 storm still exhibits some supercellular characteristics. However, its flanking line has now produced new convection southwest of the main updraft. It is difficult to discern an RFD signature in the DST2 storm at 110 min, as the reflectivity field now shows a large, single region of 40+ dBZ surrounding the main updraft. New convection is initiating just west of the main storm in both HM simulations, likely due to the strong low-level outflow associated with these systems on the back (western) sides of their forward and rear flank downdrafts. Neither the CLN1 nor the DST1 simulations produce secondary convection. All simulations exhibit a decrease in updraft size and strength from 95 to 110 min, suggesting the storms are weakening at this time.

The evolution of reflectivity at 1 km is overall similar between CLN and DST simulations of the same low-level moisture, suggesting that changing background CCN concentrations had little effect on the convection. However, assessment of the cold-pool strength between simulations suggests otherwise. The time evolution of precipitation rates on Grid 2 is shown in Figure 5. The precipitation rates in the HM cases reach maximum values near an hour into the simulations, with peak values greater than 150 mm hr^{-1}. At 65 min, the maximum rates in the LM cases are only near 50 mm hr^{-1}. Maximum values are slightly greater in the clean continental simulations, and peak precipitation rates are located within or near the RFD in all simulations at this time. After 65 min, however, the peak precipitation rates in the clean simulations are located back within the FFD region. In the DST1 supercell, peak values are located closer to the RFD.

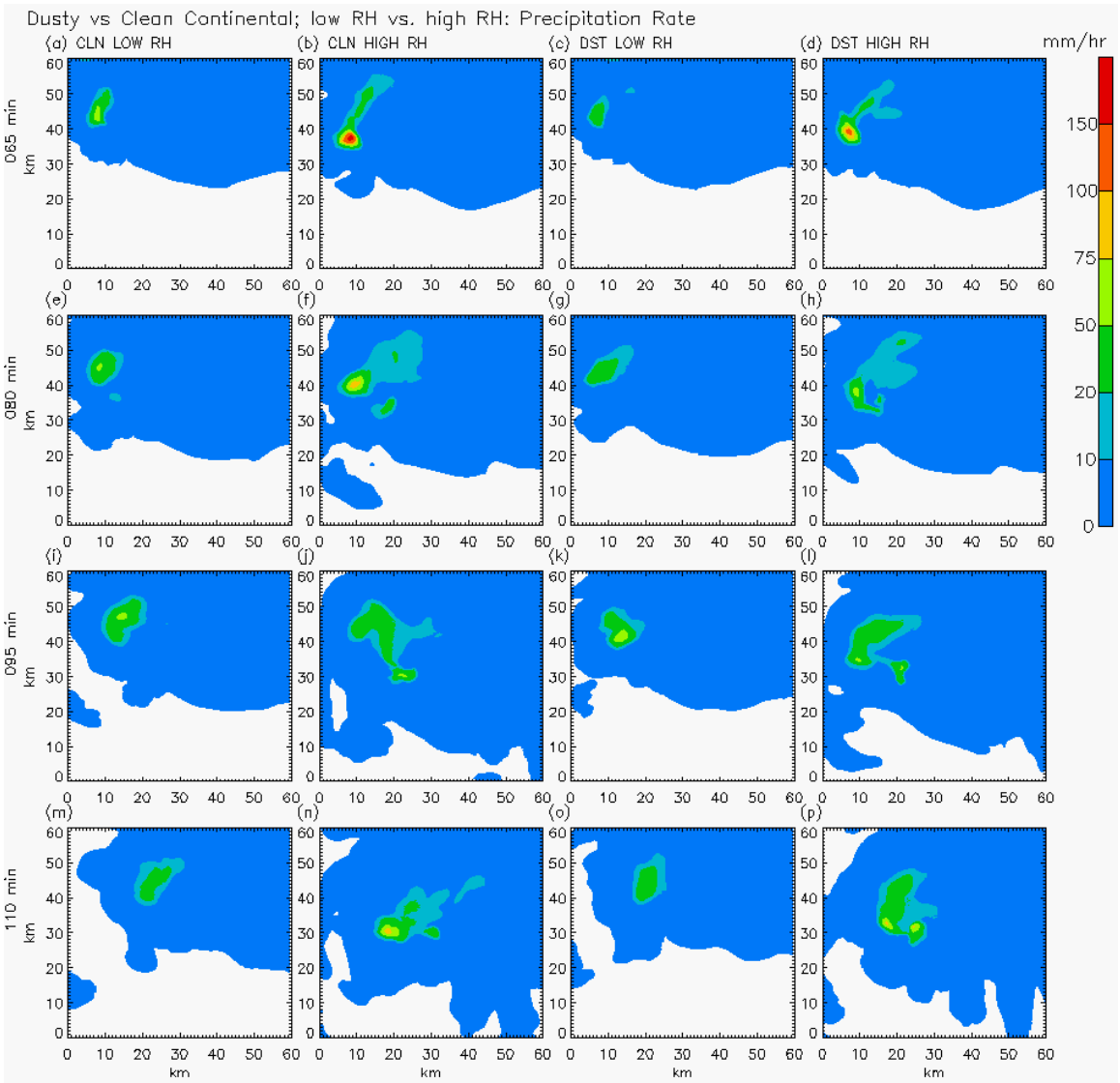

Fig. 5: Same as Fig. 3 but for precipitation rates on Grid 2.

Maximum precipitation rates generally coincide with the RFD in the DST2 storm. This suggests that both precipitation location and microphysics affected the evolution of the simulated cold-pools. Recall that the DST2 cold-pool produced the strongest temperature gradient across the RFD-based gust front even though minimum temperature values in the CLN1 cold-pool spanned a greater area.

b. Microphysical effects on Grid 2

The enhanced CCN concentrations in the dusty simulations resulted in cloud droplet concentrations that were on average 10x greater than those produced in the clean supercells (1000 vs. 100 cm^{-3} within updraft regions; not shown), and the droplets were of smaller sizes in the dusty simulations. This resulted in reduced collision efficiencies and more supercooled water aloft in the updraft regions. Figure 6 displays time series for various microphysical parameters on Grid 2. With more supercooled water aloft available for ice formation, the dusty simulations produced noticeably more (and smaller) snow and pristine ice particles than the clean simulations with the same low-level moisture (Fig. 6a). Therefore, dusty simulations produced larger, thicker anvils as more ice formation meant more ice particles forced aloft into the anvil as opposed to being used at lower levels in cold rain (rain formed from the melting of

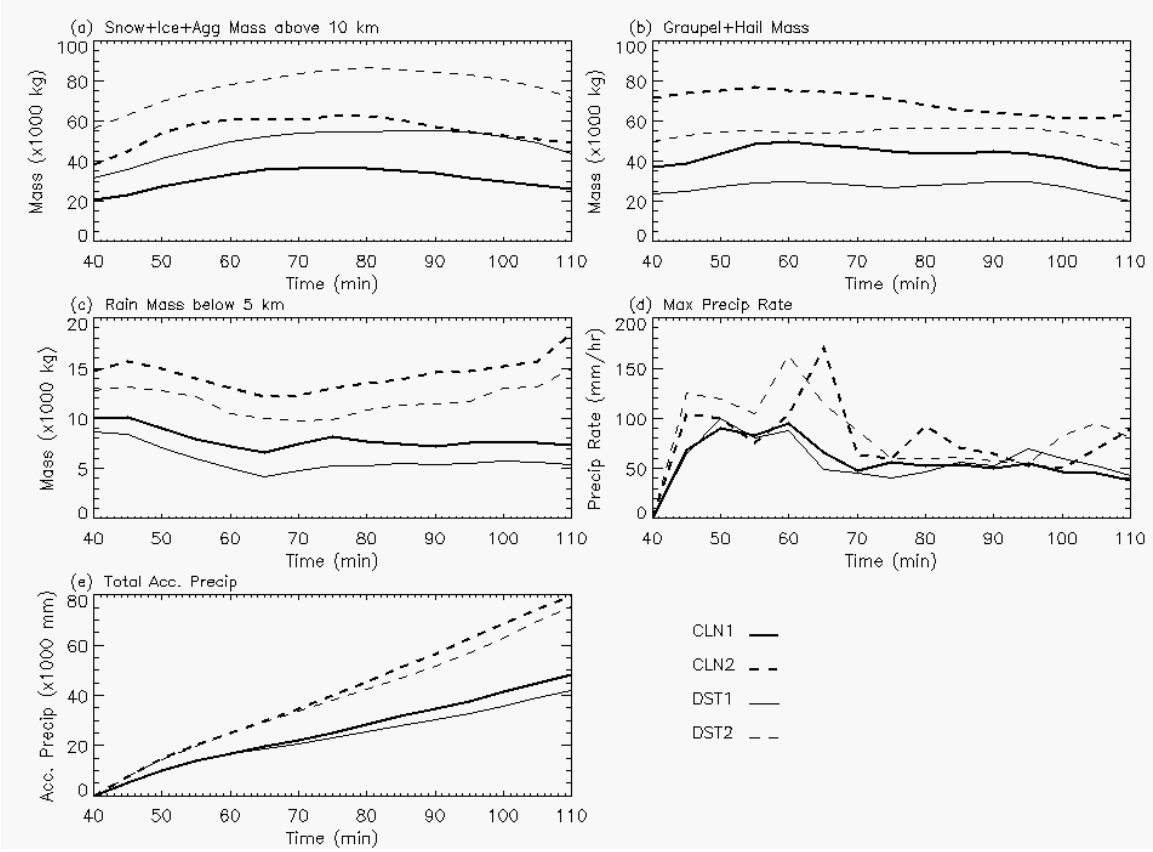

Fig. 6: Time series of domain-integrated cumulative (a) snow+pristine ice+aggregates mass above 10 km, (b) graupel+hail mass, (c) rain mass below 5 km, and (e) accumulated precipitation on Grid 2. Fig. 6d displays the time series of maximum precipitation rates on Grid 2. The thick solid, thick dashed, thin solid, and thin dashed timelines represent the CLN1, CLN2, DST1, and DST2 simulations, respectively.

graupel and hail) processes. Available low-level moisture played a contributing role as well. The HM simulations produced more ice aloft and larger anvils than the LM simulations. As such, the DST2 simulation yielded the most ice mass while the CLN1 simulation yielded the least. The CLN2 and DST1 simulations produced comparable ice mass, though values were slightly higher in the CLN2 simulation.

Figure 7 shows mean profiles of rain and hail microphysical parameters at 85 min on Grid 2. With reduced collision efficiencies, the dusty simulations produced fewer raindrops than the clean simulations. The CLN1 and CLN2 supercells produced maximum raindrop concentrations of approximately 6000 and 4000 m^{-3}, respectively, while the dusty supercells produced concentrations near 1000 m^{-3} in updrafts (Fig. 7a). However, due to the abundance of cloud drops available and higher in-cloud trajectories and thus longer net liquid water paths, the raindrops that did form were able to grow to larger sizes compared to the clean simulations (Fig. 7b). The DST2 and DST1 simulations produced raindrop median diameters of roughly 0.7 and 0.6 mm in updraft regions, respectively, while the clean simulations produced raindrops roughly 0.3 mm in diameter. Similar results were seen in the production of graupel and hail. The CLN2 and CLN1 simulations led to net maximum graupel+hail concentrations near 1800 and 1500 m^{-3}, respectively within updraft regions (Fig. 7e). The dusty simulations produced concentrations near 600 m^{-3}, but the sizes of the hailstones in these simulations were on average larger than in the clean cases. Maximum median hail diameters in updraft regions for the dusty and clean supercells were near 1 and 0.8 mm, respectively (Fig. 7f). This translated to larger graupel+hail concentrations in downdraft regions in the clean cases as well, with concentrations aloft around 1300 and 1000 m^{-3} for the CLN2 and CLN1 cases, respectively.

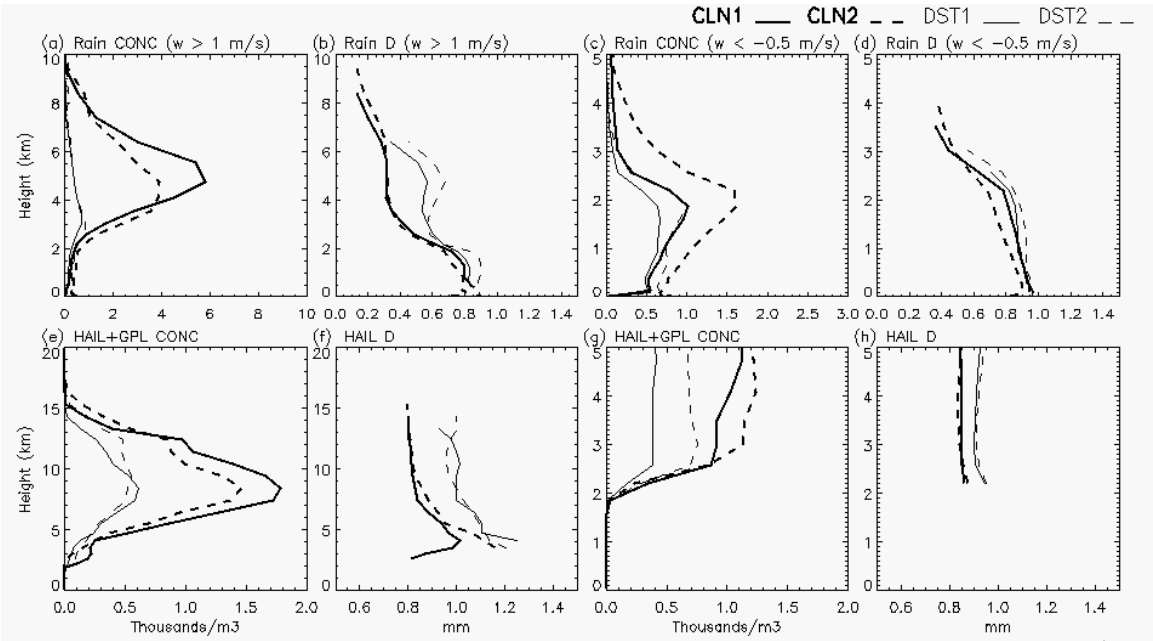

Fig. 7: Profiles of mean raindrop (a) concentrations and (b) median diameter within updraft regions (w > 1 m s^{-1}), (c) concentrations and (d) median diameter within downdrafts (w < 0.5 m s^{-1}); (e) mean hail+graupel concentrations and (f) median hailstone diameter within updraft regions (w > 1 m s^{-1}), (g) mean hail+graupel concentrations and (h) median hailstone diameter within downdrafts (w < 0.5 m s^{-1}) at 85 min on Grid 2.

Concentrations in the DST2 and DST1 cases were near 700 and 400 m^{-3}, respectively. The dusty simulations again produced larger hailstones in the downdrafts at 85 min. The dusty and clean simulations produced hailstones of 0.95 and 0.85 mm, respectively. Differences between simulations in raindrop concentrations and sizes within downdrafts were similar to those observed in updraft regions. The clean simulations produced the largest raindrop concentrations in downdrafts (1700 and 1000 m^{-3} for CLN2 and CLN1, respectively) compared to the dusty simulations (1000 and 600 m^{-3} for DST2 and DST1, respectively). Note that the HM simulations also produced more numerous raindrops than their respective LM simulations. But again, the dusty simulations produced the largest raindrops (0.9-0.95 mm) compared to the clean simulations (0.8-0.9 mm). As a result, the cleaner, higher-moisture simulations produced the most rain, graupel, and hail mass throughout the domain of Grid 2 (Fig. 6b-c). The CLN2, DST2, CLN1, and DST1 simulations produced a total of 15000, 13000, 10000, and 8500 kg worth of rain, respectively, by 40 min (Fig. 6c). In addition, the CLN2, DST2, CLN1, and DST1 simulations produced a total of 80000, 55000, 40000, and 25000 kg worth of hail and graupel, respectively at 40 min (Fig. 6b). As a result, the cleaner, higher-moisture simulations produced the most accumulated precipitation even though maximum precipitation rates were somewhat chaotic throughout the simulations (Fig. 6d-e). Though, with more moisture available for precipitation processes, the HM cases tended to yield the highest precipitation rates throughout the simulation period. Figure 8 displays accumulated precipitation on Grid 2 at 110 min for all simulations. It is apparent that the LM simulations yielded the maximum accumulated precipitation values, while the HM simulations yielded more total accumulated precipitation that was more spread out through the domain. Also, notice that the clean simulations show relative maxima of accumulated precipitation further back within the FFD, while the dusty simulations produced more accumulated precipitation within the RFD, nearer to the main updraft. As the clean supercells possessed significantly more raindrops, graupel, and hailstones of smaller sizes compared to the dusty supercells, more total surface area of precipitation particles were exposed to the air while falling through the downdrafts, leading to more evaporative

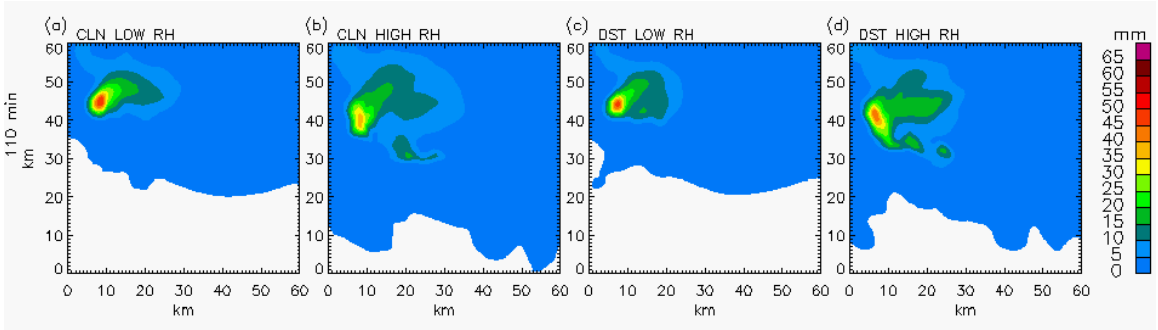

Fig. 8: Same as Fig. 3m-p but for accumulated precipitation on Grid 2 at 110 min.

cooling and thus colder, stronger downdrafts in the clean simulations. This produced larger, colder cold-pools at the surface in the clean cases compared to the dusty simulations (Fig. 4). Furthermore, the HM supercells produced significantly stronger cold-pools compared to the LM supercells, because these simulations provided for more available moisture, and therefore higher raindrop concentrations of larger sizes (on average) compared to the supercells in the LM simulations.

c. Tornadogenesis on Grid 3

Tornado-like surface vortices are produced in all four simulations, but at different times and of varying strength and longevity. The CLN1 supercell produces a surface vortex at 66 min, which dissipates at 78 min, then reforms from 81 to 82 min. The CLN2 supercell spawns a vortex at the surface from 76 to 80 min. The DST1 simulation first creates a vortex at 61 min, which then dissipates at 70 min. Lastly, the DST2 supercell produces a weak cyclonic surface circulation from 77 to 79 min. Figure 9 displays the near-surface (~24 m) temperature, vertical vorticity, perturbation pressure, and ground-relative winds (storm-relative wind vectors overlaid) on Grid 3 for all four simulations during maximum vortex intensity when a coherent, cyclonic circulation exists. At 75 min, the tornado-like vortex in the CLN1 simulation (Fig. 9a-d) coincides with maximum relative vertical vorticity near 0.2 s^{-1}, a local (within the surrounding 2x2 km of the vortex center) pressure drop of roughly 4 mb, and a strong cyclonic circulation as evident in the storm-relative wind vectors. Maximum ground-relative winds are at EF-2 intensity south and southwest of the vortex center, with maximum surface winds exceeding 50 m s^{-1} just south of the vortex. The circulation actually achieves higher vertical vorticity and a greater local pressure drop at 81 min (0.4 s^{-1} and 6 mb, respectively). However, there was no clear cyclonic circulation at the surface at this time. The cold-pool is relatively weak near the vortex, with minimum temperatures greater than 25°C immediately surrounding the vortex. Figure 9e-h displays the surface vortex produced by the CLN2 supercell at 77 min. The vortex achieves a maximum value of vertical vorticity near 0.2 s^{-1}, associated with a local pressure drop of roughly 2.5 mb. A cyclonic circulation exists at the surface, but weaker than that seen in the CLN1 simulation. The CLN2 vortex produces winds of EF-1 intensity south of the vortex center, with maximum winds reaching 41 m s^{-1}. The cold-pool west of the vortex is noticeably colder compared to that in the CLN1 case, as minimum temperatures around the CLN2 vortex reach as low as 23°C, three degrees cooler than those produced in the CLN1 simulation. Notice that in the case of the CLN1 near-vortex environment, storm-relative winds to the north and northeast of the vortex center clearly contain an easterly and a northerly component within the vicinity of the FFD, while the winds to the west and northwest contain both a northerly and westerly component within the RFD. In the CLN2 simulation, storm-relative winds north and northwest of the main vortex are straight northerly. The winds to the west are straight westerly. This suggests that the FFD and RFD are stronger in the CLN2 simulation, providing an environment less favorable for allowing warmer, less negatively buoyant air from the inflow region to the southeast to surround and enter the vortex.

The near-surface vortex in the DST1

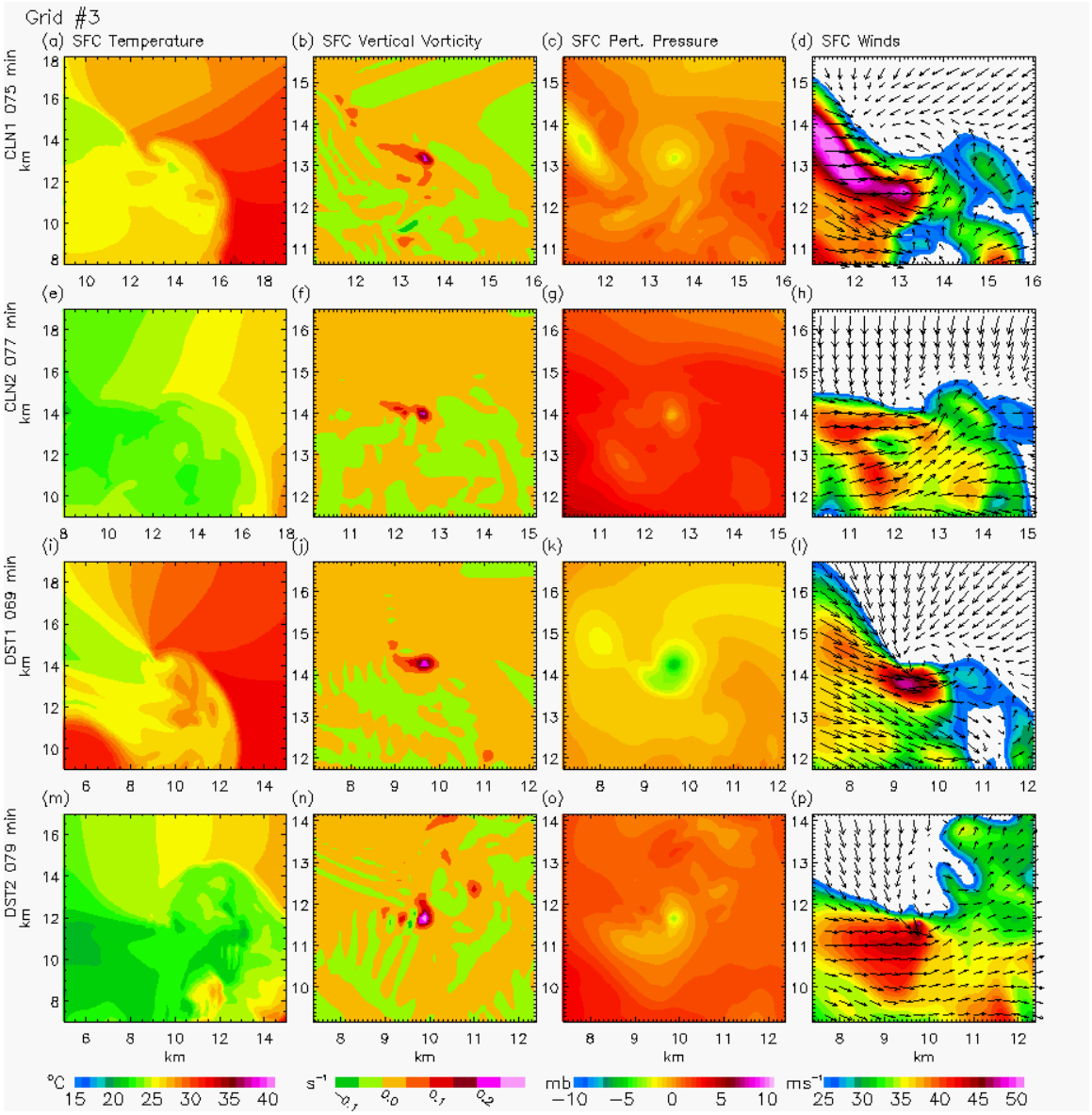

Fig. 9: Near-surface temperature, vertical vorticity, perturbation pressure, and ground-relative winds overlaid with storm-relative wind vectors in columns 1, 2, 3, and 4, respectively for Grid 3. Ground-relative winds are contoured only where ground-relative wind speeds exceed EF-0 intensity (29.2 m s^{-1}). Rows 1, 2, 3, and 4 display these variables for the CLN1, CLN2, DST1, and DST2 cases, respectively at the times of maximum near-surface vortex intensity. Note that a storm-relative wind vector represents the wind at the location of the end of its tail.

supercell (Fig. 9i-l) reaches its strongest intensity at 69 min, and compares more favorably with the vortex of the CLN1 supercell compared to that in the CLN2 experiment. Maximum vertical vorticity approaches 0.23 s^{-1}. A local pressure drop of 5 mb is achieved, and the storm-relative wind vectors indicate a strong cyclonic circulation with EF-1 ground-relative wind intensity immediately south of the vortex center. Maximum winds reach 47 m s^{-1}. The cold-pool near the vortex is of a similar structure as in the CLN1 simulation. Storm-relative winds north of the vortex contain an easterly component, while winds directly west contain a northerly component. The DST1 experiment also produces a larger region where temperatures below 25°C protrude into the western edge of the vortex circulation (Fig. 9e, light green). The DST2 simulation (Fig. 9m-p) produces a near-surface relative vertical vorticity maximum near 0.3 s^{-1} at 79 min. This vorticity maximum is associated with a local pressure

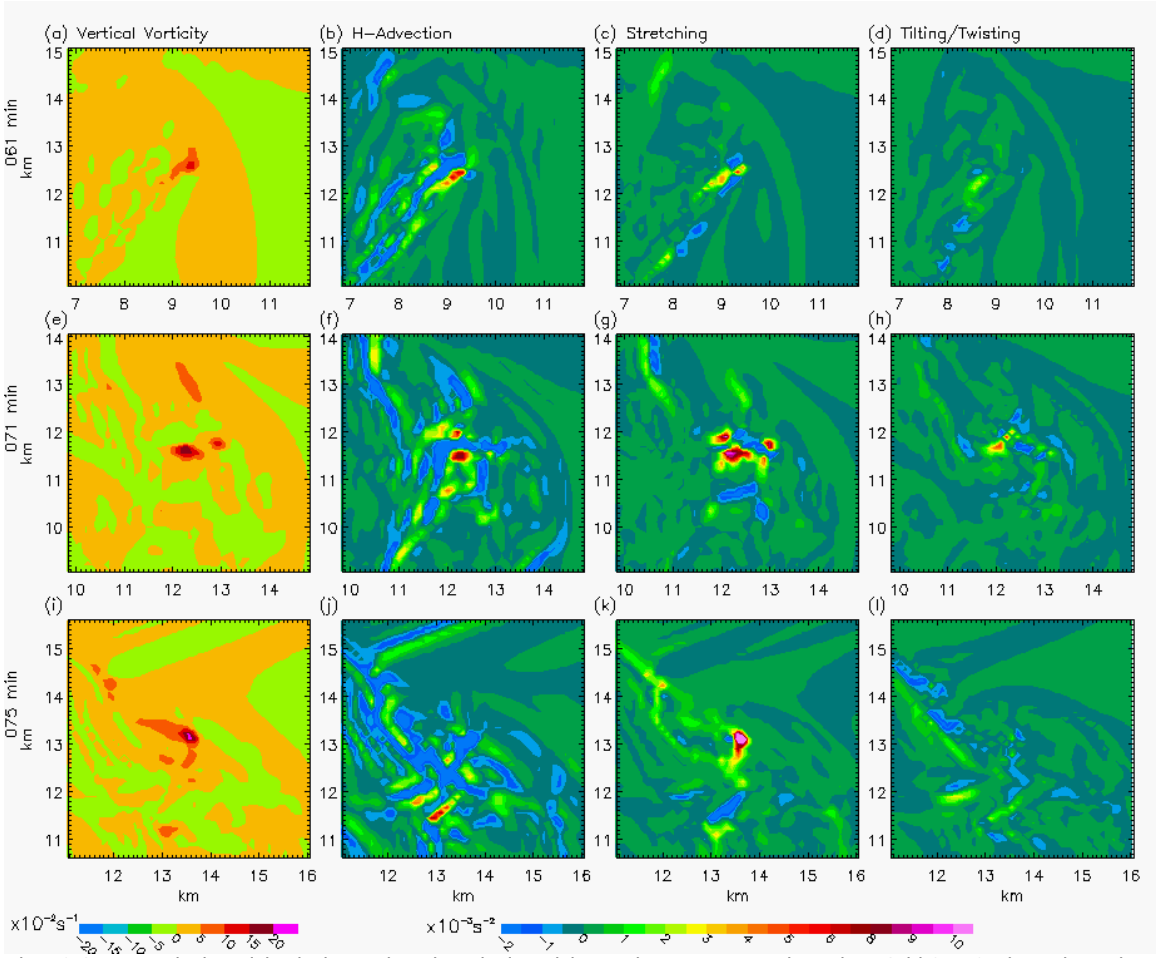

Fig. 10:CLN1 vertical vorticity (column 1) and vertical vorticity tendency terms evaluated on Grid 3 at 61 (row 1), 71 (row 2), and 75 (row 3) min: horizontal advection (column 2), vertical stretching (column 3), and twisting/tilting (column 4).

drop of approximately 3 mb and EF-1 surface winds immediately southwest of its center, where a small region of maximum ground-relative winds reach 49 m s^{-1}. A more noticeable, larger region reaches 44 m s^{-1}. The cold-pool southwest of the vortex is colder than that of the CLN2 simulation, with minimum temperatures reaching 22°C. However, minimum temperatures immediately surrounding the western and southern edges of the surface vortex are similar to those in the CLN2 simulation (23°C). The storm-relative winds associated with the outflow from the FFD and RFD are most similar to the CLN2 simulation.

The maximum ground-relative near-surface winds occur where the direction of primary vortex rotation and storm propagation coincide with the outflow from the RFD. It appears that the CLN1 and DST1 supercells produce similar vortices and similar cold-pool structures surrounding the developing vortices while the CLN2 and DST2 simulations also compare favorably. This suggests that low-level moisture played the largest role in driving the cold-pool evolution within each storm. However, differences in the time of initiation, longevity, and intensity between all four simulated vortices suggest that aerosol effects contributed to tornadogenesis as well. Next, we assess the evolution of vertical vorticity production leading up to maximum vortex intensity in order to better understand the tornadogenesis process in these simulations. Equation 1 describes the vertical vorticity time tendency equation:

$$\frac{\partial \zeta}{\partial t} = -\left(u\frac{\partial \zeta}{\partial x} + v\frac{\partial \zeta}{\partial y}\right) - w\left(\frac{\partial \zeta}{\partial z}\right) - (\zeta + f)\left(\frac{\partial u}{\partial x} + \frac{\partial v}{\partial y}\right) - \left(\frac{\partial w}{\partial x}\frac{\partial v}{\partial z} - \frac{\partial w}{\partial y}\frac{\partial u}{\partial z}\right), \quad (1)$$

where the left hand side of the equation shows the local time rate of change in the vertical vorticity. The first term on the right

hand side represents the horizontal vorticity advection. The second term represents the advection of vertical vorticity. The third term identifies the stretching term, and the last term is the tilting/twisting term. These terms were calculated at the surface within the near-vortex environment for each simulated storm. Figure 10 displays the time evolution of the horizontal advection, vertical stretching, and tilting/stretching terms for the CLN1 simulation prior to and during tornadogenesis. Near-surface vertical relative vorticity is displayed in the first column to identify the location of the primary vortex. The vertical advection term has been omitted, as it was never a dominating term. At 61 min, the horizontal advection term dominates, with maximum values near the vortex of $5x10^{-3}$ s^{-2}. The tilting/twisting and vertical stretching terms are still playing a role, with maximum values of $2x10^{-3}$ and $4x10^{-3}$ s^{-2}, respectively, near the developing surface vortex. Notice how the tilting/stretching term is slightly positive nearly wherever the vertical relative vorticity is slightly greater than 0 s^{-1}. This is consistent throughout every simulation prior to tornadogenesis (not shown). By 71 min, all three terms roughly double in value near the vortex. The horizontal advection term shows a maximum value near $8x10^{-3}$ s^{-2}, but the stretching term is now playing the largest role, with maximum values near $9x10^{-3}$ s^{-2}. The tilting/twisting term shows values around $4x10^{-3}$ s^{-2} near the vortex. When the vortex is at its strongest at 75 min, the vertical stretching term clearly dominates. In fact, the horizontal advection and tilting/twisting terms are an order of magnitude smaller than the stretching term. The vertical stretching term has maximum values greater than $10x10^{-3}$ s^{-2} around the vortex while the values of the horizontal advection and tilting/twisting terms are less than $0.5x10^{-3}$ s^{-2}. However, the tilting/twisting term remains slightly positive throughout the region. It appears that prior to and at tornadogenesis, the tilting/twisting term is contributing to the creation of low-level vertical vorticity, though the degree to which this process is producing vertical vorticity compared to the ambient mesoscale environment and the downward vertical advection of vertical vorticity by the RFD has not been quantified. Nevertheless, the near-

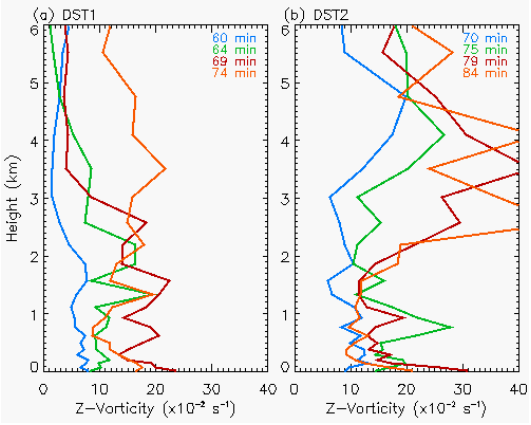

Fig. 11: Vertical profiles of maximum relative vertical vorticity on Grid 3 for the (a) DST1 and (b) DST2 simulations. The surface vortex in the DST1 and DST2 simulations are most coherent at 69 and 79 min, respectively.

surface vortex appears to be initially concentrated by the horizontal advection term. This is consistent with the results of Gaudet and Cotton (2006) and Gaudet et al. (2006). Then as expected, the vortex reaches tornadic intensity through vertical stretching. Gaudet and Cotton (2006) and Gaudet et al. (2006) used a similar idealized setup and initial sounding in RAMS as this study to create a tornadic supercell, which produced a tornado-like vortex at the surface initially through barotropic-like 2D processes, where the vortex was initially formed by the horizontal rearrangment of vertical vorticity. Figure 11 displays vertical profiles of maximum relative vertical vorticity at various times for the DST1 (Fig. 11a) and DST2 (Fig. 11b) simulations on Grid 3 within the 3x3 km region surrounding the primary vortex. The blue, green, red, and orange profiles represent the maximum vertical vorticity 10 min prior, 5 min prior, at, and 5 min after peak surface vortex intensity for both simulations, respectively. Recall that Grid 3 was initialized at 60 min. Therefore, the blue profile in the DST1 simulation represents a time of 9 min prior to maximum vortex intensity. The near-surface vertical vorticity increases slightly from 60 to 64 min in the DST1 case. Vertical vorticity then increases noticeably between 64 and 69 min, from 0.09 to 0.24 s^{-1}. By 74 min, the maximum vertical vorticity at the surface drops to 0.17 s^{-1}. At 60 min, vertical vorticity remains greater than 0.005 s^{-1} from the surface up to roughly 2 km. At 64 min, the largest values are below 2.3 km. By 69 min,

values do not decrease with height until 2.7 km. By 74 min, vertical vorticity increases from 0.05 to values greater than 0.15 s^{-1}. This evolution suggests that the vortex initially forms at the surface and builds upward with time by advecting vertical vorticity upward. A similar evolution is seen in the DST2 case from 70 to 84 min. However, the vertical vorticity was initially stronger aloft in the DST2 experiment compared to the DST1 simulation (0.2 vs. 0.04 s^{-1}, respectively), due to the fact that the HM (and thus higher CAPE) simulations produced the strongest mesocyclones.

The overall surface pressures near the vortices of interest are higher in the HM experiments, as they produce stronger, colder outflow throughout the duration of the simulations. The LM cases produce stronger, more concentrated vortices, as evident by the temperature data (Fig. 9, column 1). The HM supercells create stronger outflows surrounding the vortex, associated with stronger ground-relative winds east of the primary vortices (Fig. 9, column 4). Consequently, the strength and longevity of the resulting vortex and its cyclonic circulation appear to be related to the strength of the surrounding cold-pool produced by the FFD and RFD. Markowski et al. (2002, 2003) found that the cold-pool played a significant role in changing the buoyancy near the vortex, where supercells producing the stronger, longer lived tornado-like vortices were associated with higher CAPE and lower convective inhibition (CIN) within the near-vortex environment. CAPE and CIN were calculated for each simulation herein within the 10x10 km regions surrounding the developing primary vortices using equations 2 and 3, respectively.

$$CAPE = -R_d \int_{p_{LFC}}^{p_{EL}} \left(\theta_p - \bar{\theta}\right)\left(\frac{p}{p_o}\right)^{R_d/c_p} d\ln p \quad (2)$$

$$CIN = -R_d \int_{p_{sfc}}^{p_{LFC}} \left(\bar{\theta} - \theta_p\right)\left(\frac{p}{p_o}\right)^{R_d/c_p} d\ln p \quad (3)$$

CIN was calculated up to a level of 500 mb if there was no CAPE at a given point. CAPE and CIN are displayed in Figure 12 for all four simulations 5 min prior to those time periods shown in Fig. 9. It is clear that the two strongest tornado-like vortices (CLN1, DST1) were associated with regions of high CAPE (> 1200 J kg^{-1}) surrounding the vortex and relatively low values of CIN (< 400 J kg^{-1}). In particular, it appears that the stronger tornado-like vortices allowed relatively warm inflow air to cyclonically wrap around and surround the vortex, thus separating the stronger cold-pool air further from the vortex during peak intensity. This is evident in the temperature fields shown in Fig. 9 (column 1) and in the structure of the storm-relative wind fields (Fig. 9, column 4). Recall that the HM experiments, which produced stronger outflow from the FFD and RFD, were associated with straight northerly winds north and northwest of the vortex and westerly winds to the west. The LM storms that produced stronger vortices were associated with weaker outflows and thus larger cyclonic circulations surrounding the primary vortex, allowing less negatively buoyant inflow air from the southeast to surround the vortex. The HM cases showed no CAPE within the vicinity of the vorticity maximum during peak intensity. Likewise, CIN values were extremely high compared to the low-moisture cases near the vortex, with values greater than 2000 J kg^{-1}. This supports the findings of Markowski et al. (2002, 2003), which suggested that the intensity and longevity of a tornadic circulation is related the degree of negative buoyancy associated with the near-vortex environment. These findings fit within the observed ranges of CAPE and CIN values reported by Markowski et al. (2002) (note that CAPE was only calculated up to 500 mb in their study).

d. Isolating low-level moisture effects

The results of Markowski et al. (2002, 2003) indicated that higher ambient relative humidity at low levels was associated with the coldness of the resulting RFD, as high boundary layer relative humidity was more conducive to higher buoyancy environments for vortex development. The previous sections described how the HM simulations created the strongest, coldest RFDs, contrary to Markowski et al. (2002, 2003). However, our simulations differed in both low-level moisture and environmental CAPE. The simulations presented by Markowski et al. (2003) did not. They instead altered the

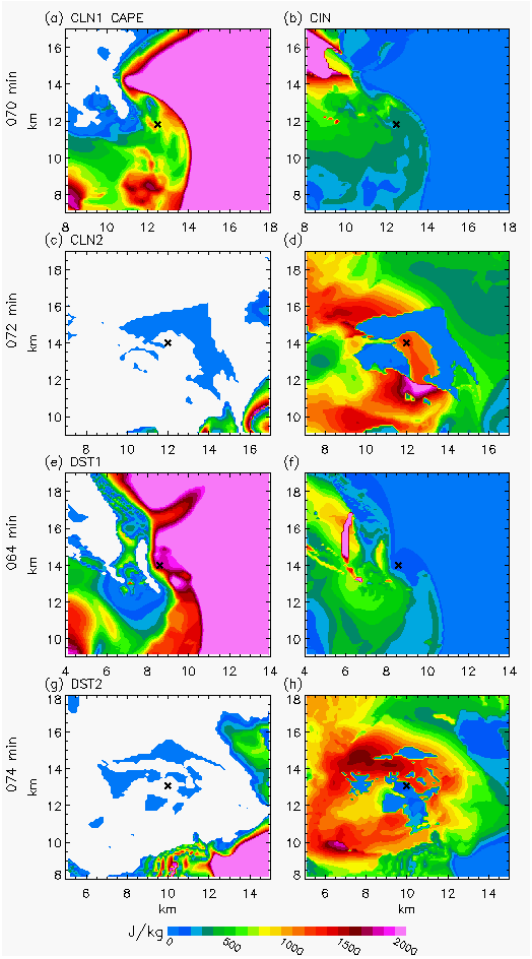

Fig. 12: CAPE (column 1) and CIN (column 2) calculated on Grid 3 five minutes before peak surface vortex intensity for the CLN1 (row 1), CLN2 (row 2), DST1 (row 3), and DST2 (row 4) simulations. The 'x' symbol depicts the location of the developing vortex for each simulation.

background temperature profile in order to maintain similar CAPE values between simulations. This makes it difficult to draw direct comparisons between the results of this study and those of Markowski et al. (2003) when it comes to the effects of low-level moisture on tornadogenesis. Therefore, another nested grid simulation was set up, where the initial sounding used to generate convection contained the low-level moisture profile of the HM simulations, but maintained the weaker CAPE of the LM simulations. This required increasing the temperatures of the initial sounding above 700 mb, which in turn slightly altered the ambient relative humidity profile aloft. The background aerosols were set to the clean continental values used in the CLN1 and

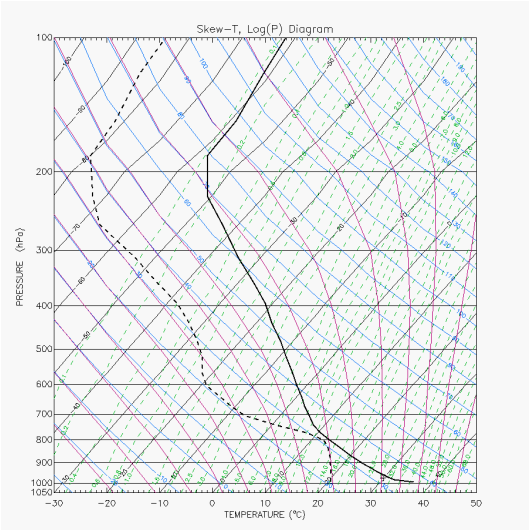

Figure 13: Skew T-log p diagram of initial background temperature and dew point temperature profiles for the CLN2b simulation.

CLN2 simulations. The results from this simulation, hereafter referred to as CLN2b, were compared to those of the CLN1 and CLN2 experiments in order to better understand how the aerosol-CCN effect compared to the influences of low-level moisture found previously by Markowski et al. (2003). The initial sounding used to initialize the CLN2b experiment is displayed in Figure 13 as a skew T-log p diagram.

The CLN2b experiment produces a local maximum in near-surface vertical vorticity from 63 to 69 min. The vorticity center reaches a maximum value of 0.32 s^{-1} at 64 min. However, the vorticity center is not associated with a clear cyclonic circulation at this time. The vortex is associated with a cyclonic circulation between 65 and 69 min. Figure 14 shows the near-surface (~24 m) temperature, vertical relative vorticity, perturbation pressure, and ground-relative winds (storm-relative wind vectors overlaid) for the CLN1 (row 1), CLN2b (row 2), and CLN2 (row 3) simulations on Grid 3 at 75, 66, and 77 min, respectively. The CLN2b vortex is associated with a cyclonic circulation and a maximum vertical vorticity value of 0.18 s^{-1}. The vortex contains a 3-mb local pressure drop. Ground-relative winds are near 40 m s^{-1} immediately south of the vortex. However, as with the CLN2 and DST2 simulations, the maximum surface winds are located in the vicinity of the RFD-based outflow region southeast of the main vortex.

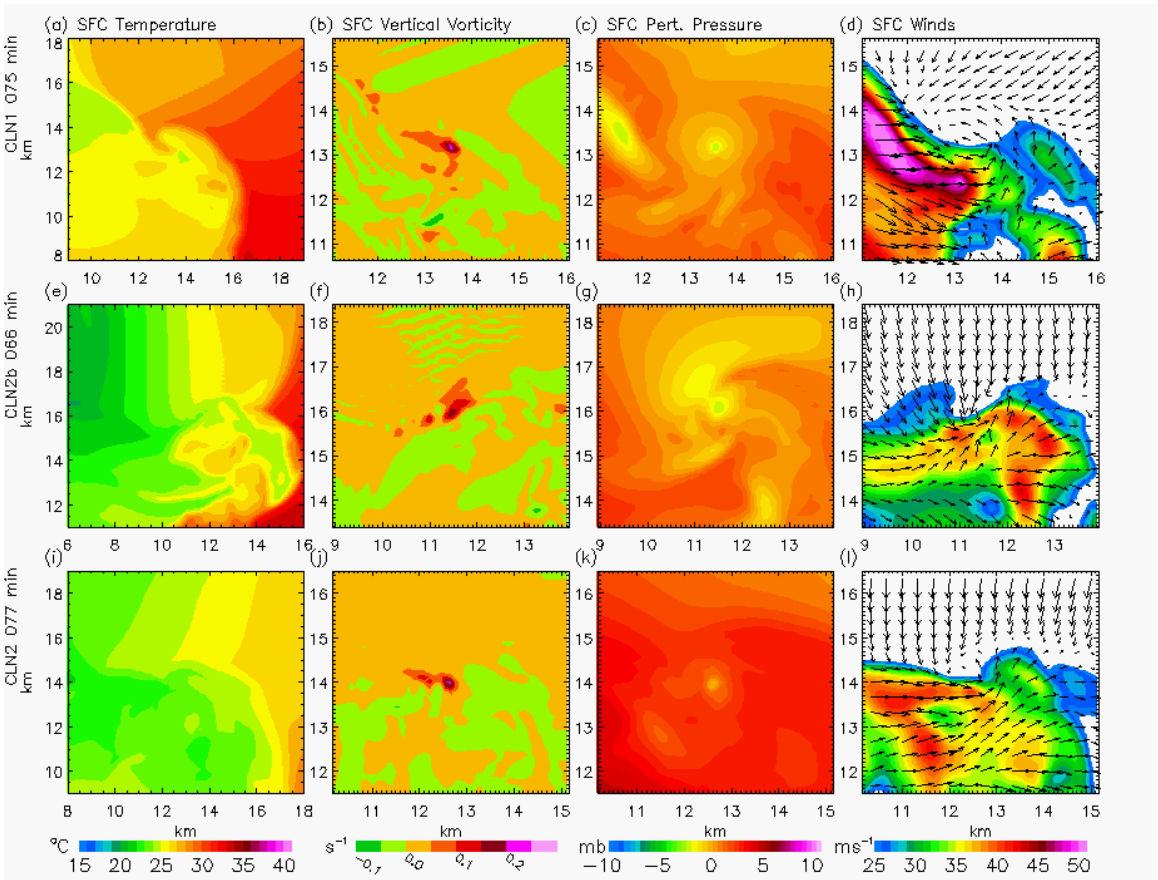

Fig. 14: Same as Fig. 9 but for the CLN1 simulation at 75 min (row 1), the CLN2b (row 2) simulation at 66 min, and the CLN2 (row 3) simulation at 77 min.

Here, wind speeds exceed 44 m s^{-1}. Furthermore, the near-surface winds north and northwest of the vortex are strongly northerly. The cold-pool west of the vortex reaches a minimum temperature value of 19°C. However, the region directly surrounding the vortex contains temperature values only as low as 23°C. While all three simulations result in slightly different cold-pool strengths and positions relative to the developing vortex, it appears that the vortex that forms in the CLN2b simulation compares more favorably with that of the CLN2 simulation than the CLN1 experiment. These simulations yield similar FFD- and RFD-based cold-pool structures, ground-relative wind fields, and near-vortex pressure falls. Figure 15 displays precipitation rates on Grid 2 at 65 min for the CLN1, CLN2, and CLN2b experiments. 3.5-km vertical velocity is overlaid. The CLN1 supercell produces relatively weak precipitation rates at this time, with a core containing precipitation rates less than 75 mm hr^{-1} back within the FFD (Fig. 15a). The CLN2 supercell produces weak precipitation within its FFD but precipitation rates greater than 150 mm hr^{-1} within the RFD (Fig. 15b). However, this precipitation core is located approximately 4 km west of the main updraft core under which tornadogenesis occurs. Meanwhile, the CLN2b supercell produces a precipitation core within the FFD that is larger than either core produced by the CLN1 or CLN2 simulations, with maximum precipitation rates that are greater than 100 mm hr^{-1}. In the CLN2b simulation, however, the precipitation core is immediately adjacent to the main updraft. The main updraft is noticeably smaller and slightly weaker in the CLN2b case compared to the CLN1 and CLN2 experiments. Consequently, the CLN2b simulation produced a slightly stronger cold-pool near the developing surface vortex compared to the CLN2 simulation (Fig. 14, column 1). Note that the CLN2 supercell contained a noticeably stronger mid-level mesocyclone compared to that of the CLN1 and CLN2b simulations (not shown) due to the presence

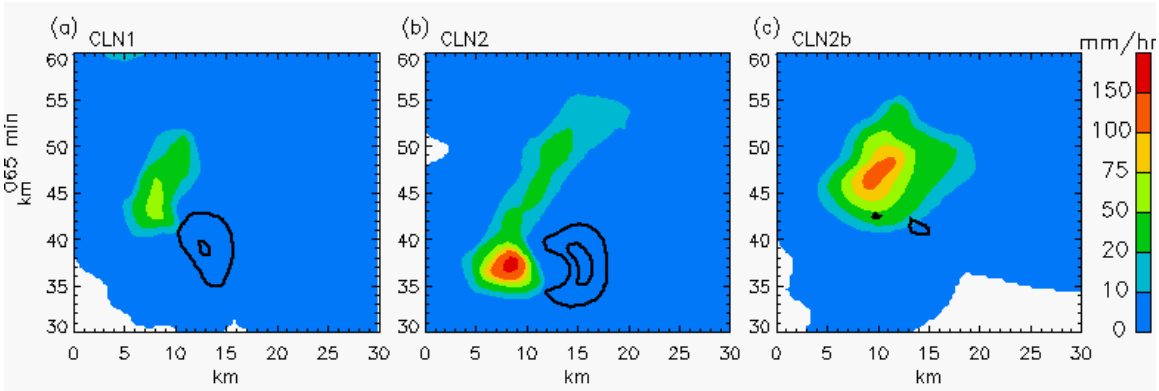

Fig. 15: Precipitation rates on Grid 2 for the (a) CLN1, (b) CLN2, and (c) CLN2b simulations at 65 min. 3.5-km updrafts are overlaid and contoured at 10 and 20 m s^{-1}.

of significantly larger environmental CAPE. The stronger mesocyclone allowed for more precipitation to be wrapped cyclonically around the main updraft to the RFD in the CLN2 experiment, while more precipitation was able to fall within the FFD in the CLN2b supercell.

The findings of the CLN2b simulation, when compared to those of the CLN1 and CLN2 simulations, indicated that increasing the ambient relative humidity profile at low levels without affecting CAPE still resulted in a colder, stronger cold-pool that created a less favorable environment for tornadogenesis. This is in contrast to the idealized simulations by Markowski et al. (2003) that suggested that increasing the ambient low-level relative humidity provided a more favorable situation for tornadogenesis. This difference in findings is due to the parameterizations used in the Markowski et al. (2003) model setup. In their different simulations, the ambient relative humidity was increased below 720 mb. However, the amount of precipitation remained constant. As a result, the increased relative humidity led to reduced evaporative cooling, a weaker cold-pool, and a more favorable environment for tornadogenesis. In the three-dimensional, less idealized simulations performed for this study, precipitation was not held fixed between simulations. The increased relative humidity at low levels meant an increased moisture supply available for precipitation processes. Therefore, the simulation with increased relative humidity below 800 mb produced significantly stronger precipitation cores compared to the simulation initialized with lower relative humidity. The heavier precipitation resulted in enhanced evaporative cooling, stronger downdrafts, and stronger, colder cold-pools, which created a less favorable environment for vortex development.

4. Discussion

An ensemble of five simulations, using RAMS, was performed to compare the effects of CCN and low-level moisture on tornadogenesis. Each simulation produced splitting supercells, with the right mover becoming tornadic between 60 and 80 min. While each simulated supercell evolved in a similar manner, large differences were found with respect to storm microphysics and low- to mid-level dynamics. Increasing the ambient low-level moisture profile below 800 mb without altering the ambient temperature profile created significantly higher environmental CAPE. The combined effect was to produce larger storms with stronger peak updrafts and stronger low-level downdrafts compared to the LM simulations. The HM simulations produced storms with significantly stronger precipitation rates and higher accumulated precipitation, which resulted in higher evaporative cooling rates and thus larger, colder, and stronger cold-pools at the surface associated with both the forward and rear flank downdrafts. The storms in the HM simulations showed more precipitation wrapping cyclonically around the main updraft as it fell through the RFD, due to the greater strength of the mid-level mesocyclone in the HM cases. Essentially, the LM simulations produced storms that behaved primarily like “classic” supercells, while the storms in the HM simulations

exhibited some characteristics of high-precipitation (HP) type supercells. The higher CCN concentrations in the dusty simulations created higher cloud droplet concentrations but of smaller sizes compared to the clean continental simulations. This reduced collision and coalescence, resulting in fewer raindrops and a reduction in warm rain production. However, with more supercooled water aloft and longer vertical trajectories by raindrops in-cloud, the raindrops that did form generally grew to larger sizes than those in the clean continental simulations, and the dusty simulations produced noticeably larger, thicker anvils. The dusty simulations also resulted in lower graupel and hail concentrations. However, with slightly stronger updrafts and more available cloud water for riming, hailstones grew to larger sizes compared to the clean continental simulations. With fewer but larger raindrops, graupel particles, and hailstones, the supercells from the dusty simulations underwent less evaporative cooling within downdrafts, and thus produced weaker, warmer cold-pools compared to the clean simulations. However, with greater terminal fall velocities, the larger hydrometeors fell nearer to the storm's core, which positioned the cold-pool closer to the main updraft. These results are consistent with those of Storer et al. (2010).

The tornado-like vortices that developed in each simulation appeared to have initially formed at the surface, primarily via the horizontal advection of vertical vorticity, then build upward to merge with the low- and mid-level mesocyclones. Enhanced vertical stretching then strengthened the vortex to tornadic intensity. Gaudet et al. (2006) described a similar process to the development of a surface vortex within a similar numerical setup, where the vortex initially formed primarily via two-dimensional processes through the horizontal rearrangement of vertical vorticity. With regard to this study, it is unclear as to how great a role the RFD played in creating ambient horizontal vorticity and transporting vertical vorticity to the surface. However, tornadogenesis was related to the size, strength, and location of the FFD- and RFD-based cold-pools. The combined influence of low-level moisture and CAPE played a noticeably larger role to the tornadogenesis process compared to the aerosol influence. However, the aerosol effect was still evident. Changing the low-level moisture profile resulted in changes to storm size and precipitation totals, but altering the background available CCN concentrations resulted in significant differences in storm microphysics and the location of precipitation cores. It was the combined effect that determined the strength and location of the cold-pool. The LM simulations produced the weakest cold-pools and were most favorable for tornadogenesis, as they were associated with less negative buoyancy than the HM simulations. The results of the LM simulations differ somewhat from those of Lerach et al. (2008), which indicated that the CCN-polluted environment was more favorable for tornadogenesis. The CLN1 near-vortex environment at low levels was actually more favorable for tornadogenesis than that of the DST1 simulation, as the CLN1 FFD- and RFD-associated outflow possessed warmer temperatures and less negative buoyancy (stronger CAPE and weaker CIN) than that of the DST1 simulation at the time of vortex development. Note that an earlier version of RAMS microphysics was utilized in the Lerach et al. (2008) simulations (Saleeby and Cotton 2004). Those simulated storms produced considerably higher precipitation rates and evaporative cooling rates within the FFD and RFD, resulting in considerably stronger cold-pools and associated outflow. The clean continental simulation produced an FFD-based cold-pool strong enough to undercut the storm's core before a surface-based vortex could develop. This was not the case in the current set of simulations. The results from the CLN1 and DST1 simulations differed from those of Snook and Xue (2008) in that their simulations suggested that tornado potential increased as the cold-pools weakened. The CLN1 simulation produced a stronger cold-pool than the DST1 simulation overall. However, the cold-pool in the DST1 simulation was closer to the developing vortex at the time of tornadogenesis than that in the CLN1 experiment, and thus colder, more negatively buoyant air surrounded the vortex. On the other hand, the CLN2 and DST2 simulations produced cold-pools of comparable strength at the time of

tornadogenesis, at least within the near-vortex environment. As a result, the DST2 simulation actually produced a stronger near-surface vortex than that of the CLN2 experiment. Notice that the vortex in the DST2 simulation was associated with lower values of CIN compared to the CLN2 simulation (Fig. 12d,h). It should be noted that no significant differences in surface convergence within the near-vortex environment were found between the CLN1, CLN2, DST1, and DST2 simulations immediately prior to or during tornadogenesis.

The sounding used to initialize the CLN2b experiment was set up with the relative humidity profile below 800 mb of the HM simulations, while maintaining the CAPE of the LM simulations. With an increased supply of available low-level moisture, the supercell that developed still produced significantly stronger precipitation than the LM simulations, which produced more evaporative cooling within downdraft regions, and thus stronger, colder cold-pools at the surface. This resulted in a weaker, shorter-lived surface vortex compared to the LM simulations. With stronger outflow, lower CAPE, higher CIN, and thus greater negative buoyancy, the simulation with higher ambient relative humidity below 800 mb provided a less favorable environment for tornadogenesis. While these findings contradict those of Markowski et al. (2003) due to their precipitation parameterization, their general results were consistent with those of this study. *The strongest, longest-lived vortices were associated with warmer and weaker cold-pools, higher CAPE, lower CIN, and thus less negative buoyancy in the near-vortex environment compared to those storms that produced shorter-lived, weaker vortices.*

These findings are based on a single thermodynamic sounding, and surface friction was not considered. Further investigation is required to address the robustness of the results presented herein.

Acknowledgments

Thanks to Dr. Susan van den Heever of CSU for her insight regarding this work. Also, we thank Drs. Louie Grasso of CIRA and Brian Gaudet of PSU for their assistance in setting up the simulations. This work was funded by National Science Foundation (NSF) Grant ATM-0638910.

References

Arakawa, A., and V. Lamb, 1981: A potential enstrophy and energy conserving scheme for the shallow water equations. *Mon. Wea. Rev.,* **109,** 18–36.

Braham, R. R., Jr., R. G. Semonin, A. H. Auer, S. A. Changnon Jr., and J. M. Hales, 1981: Summary of urban effects on clouds and rain. METROMEX: A review and summary, *Meteor. Monogr.,* **40***,* Amer. Meteor. Soc., 141-152.

Brandes, E. A., 1978: Mesocyclone evolution and tornadogenesis: Some observations. *Mon. Wea. Rev.,* **106,** 995–1011.

Brooks, H. E., C. A. Doswell III, and R. B. Wilhelmson, 1994: The role of midtropospheric wind in the evolution and maintenance of low-level mesocyclones. *Mon. Wea. Rev.,* **122,** 126–136.

Burgess, D. W., R. A. Brown, L. R. Lemon, and C. R. Safford, 1977: Evolution of a tornadic thunderstorm. Preprints, *10th Conf. On Severe Local Storms,* Omaha, NE, Amer. Meteor. Soc., 84–89.

Clark, T. L., and R. D. Farley, 1984: Severe downslope windstorm calculations in two and three spatial dimensions using anelastic interactive grid nesting: A possible mechanism for gustiness. *J. Atmos. Sci.,* **41,** 329–350.

Cotton, W., R. A. Pielke Sr., R. L. Walko, G. E. Liston, C. J. Tremback, H. Jiang, R. L. McAnelly, J. Y. Harrington, M. E. Nicholls, G. G. Carrio, and J. P. McFadden, 2003: Rams 2001: Current status and future directions. *Meteor. Atmos. Phys*., **82**, 5-29.

Davies-Jones, R. P., 1982a: A new look at

the vorticity equation with application to tornadogenesis. Preprints, *12th Conf. on Severe Local Storms,* San Antonio, TX, Amer. Meteor. Soc., 249–252.

Davies-Jones, R. P., 1982b: Observational and theoretical aspects of tornadogenesis. *Intense AtmosphericVortices,* L. Bengtsson and J. Lighthill, Eds., Springer-Verlag, 175–189.

Davies-Jones, R. P., 2000: Can the hook echo instigate tornadogenesis barotropically? Preprints, *20th Conf.on Severe Local Storms,* Orlando, FL, Amer. Meteor. Soc., 269–272.

Davies-Jones, R. P., and H. E. Brooks, 1993: Mesocyclogenesis from a theoretical perspective. *The Tornado: Its Structure, Dynamics, Prediction, and Hazards, Geophys. Monogr.,* **79**, Amer. Geophys. Union, 105–114.

Eagan, R. C., P. V. Hobbs, and L. F. Radke, 1974: Particle emissions from a large Kraft paper mill and their effects on the microphysical structure of warm clouds. J. Appl. Meteor., **13**, 535-552.

Eskridge, R. E., and P. Das, 1976: Effect of a precipitation-driven downdraft on a rotating wind field: A possible trigger mechanism for tornadoes? *J. Atmos. Sci.,* **33,** 70–84.

Foote, G. B., 1984: A study of hail growth utilizing observed storm conditions. *J. Climate Appl. Meteor*., **23**, 84-101.

Gaudet, B.J., and W.R. Cotton, 2006: Low-level mesocyclonic concentration by non-axisymmetric processes. Part I: Supercell and mesocyclone evolution. J. Atmos. Sci., 63, 1113-1133.

Gilmore, M. S., J. M. Straka, and E. N. Rasmussen, 2004: Precipitation uncertainty due to variations in precipitation particle parameters within a simple microphysics scheme. *Mon. Wea. Rev.*, **132,** 2610-2627.

Grasso, L. D., 2000: The dissipation of a left-moving cell in a severe storm environment. *Mon. Wea. Rev.,* **128,** 2797–2815.

Grasso L. D. and W. R. Cotton, 1995: Numerical simulation of a tornado vortex. *J. Atmos. Sci.,* **52,** 1192–1203.

Hobbs, P. V., L. F. Radke, and S. E. Shumway, 1970: Cloud condensation nuclei from industrial sources and their apparent influence on precipitation in Washington State. *J. Atmos. Sci.*, **27**, 81-89.

Kaufman, Y. J., and T. Nakajima, 1993: Effect of Amazon smoke on cloud microphysics and albedo: Analysis from satellite imagery. *J. Appl. Meteor.*, **32**, 729-744.

Klemp, J. B., and R. B. Wilhelmson, 1978a: The simulation of three-dimensional convective storm dynamics. *J. Atmos. Sci.,* **35,** 1070–1096.

Klemp, J. B., and R. B. Wilhelmson, 1978b: Simulations of right- and left-moving storms produced through storm splitting. *J. Atmos. Sci.,* **35,** 1097–1110.

Koehler K. A., S. M. Kreidenweis, P. J. DeMott, M. D. Petters, A. J. Prenni, C. M. Carrico, 2009: Hygroscopicity and cloud droplet activation of mineral dust aerosol, Geophys. Res. Lett., 36, L08805, doi:10.1029/2009GL037348.

Lemon, L. R., 1974: Interaction of two convective scales within a severe thunderstorm: A case study. NOAA Tech. Memo. ERLNSSL, **71**, 43 pp. [NTIS COM-74-11642/AS.]

Lemon, L. R., and C. A. Doswell, 1979: Severe thunderstorm evolution and mesocyclone structure as related to

tornadogenesis. *Mon. Wea. Rev.,* **107,** 1184–1197.

Lerach, D. G., B. J. Gaudet, and W. R. Cotton, 2008: Idealized simulations of aerosol influences on tornadogenesis. *Geophys. Res. Lett*., **35**, L23806, doi:10.1029/2008GL035617.

Leslie, L. M., and R. K. Smith, 1978: The effect of vertical stability on tornadogenesis. *J. Atmos. Sci.,* **35,** 1281–1288.

Ludlam, F. H., 1963: Severe local storms: A review. *Severe Local Storms, Meteor. Monogr.,* **27**, *Amer. Meteor. Soc*., 1–30.

Markowski, P.M., 2002: Hook echoes and rear-flank downdrafts: A review. *Mon. Wea. Rev.*, **130**, 852- 876.

Markowski, P. M., J. M. Straka, and E. N. Rasmussen, 2002: Direct surface thermodynamic observations within the rear-flank downdrafts of nontornadic and tornadic supercells. *Mon. Wea. Rev.,* **130,** 1692– 1721.

Markowski, P. M., J. M. Straka, and E. N. Rasmussen, 2003: Tornadogenesis resulting from the transport of circulation by a downdraft: Idealized numerical simulations. *J. Atmos. Sci*., **60**, 795-823.

Nelson, S. P., 1977: Rear flank downdraft: A hailstorm intensification mechanism. Preprints, *10th Conf. on Severe Local Storms,* Omaha, NE, Amer. Meteor. Soc., 521–525.

Pielke, R. A., and Coauthors, 1992: A comprehensive meteorological modeling system -RAMS. *Meteor. Atmos. Phys*., **49**, 69-91.

Ray, P. S., B. C. Johnson, K. W. Johnson, J. S. Bradberry, J. J. Stephens, K. K. Wagner, R. B. Wilhelmson, and J. B. Klemp, 1981: The morphology of several tornadic storms on 20 May 1977. *J. Atmos. Sci.,* **38,** 1643–1663.

Rosenfeld, D., 1999: TRMM observed first direct evidence of smoke from forest fires inhibiting rainfall. *Geophys. Res. Lett*., **26**, 3105-3108.

Rosenfeld, D., 2000: Suppression of rain and snow by urban and industrial air pollution. *Science*, **287**, 1793-1796.

Rotunno, R., and J. B. Klemp, 1982: The influence of the shear induced pressure gradient on thunderstorm motion. *Mon. Wea. Rev.,* **110,** 136–151.

Saleeby, S. M., and W. R. Cotton, 2004: A large droplet mode and prognostic number concentration of cloud droplets in the Colorado State University Regional Atmospheric Modeling System (RAMS). Part I: Module descriptions and supercell test simulations. *J. Appl. Meteor.*, 43, 182-195.

Saleeby, S. M., and W.R. Cotton, 2008: A binned approach to cloud droplet riming implemented in a bulk microphysics model. *J. Appl. Met*. *Climatol.*, **47**, 694-703.

Seifert, A. and K. D. Beheng, 2006: A two-moment cloud microphysics parameterization for mixed-phase clouds. Part II: Maritime vs. continental deep convective storms, *Meteorol. and Atmos. Phys.*, **92**, 67-82.

Snook, N., and M. Xue, 2008: Effects of microphysical drop size distribution on tornadogenesis in supercell thunderstorms. *Geophys. Res. Lett.,* **35**, L24803, doi:10.1029/2008GL035866.

Storer, R. L., S. van den Heever, and G. L. Stephens, 2010: Modeling aerosol impacts on convective storms in different environments. *J. Atmos. Sci*., accepted.

Trapp, R. J., and B. F. Fiedler, 1995:

Tornado-like vortexgenesis in a simplified numerical model. *J. Atmos. Sci.,* **52,** 3757–3778.

Tripoli, G. J., and W. R. Cotton, 1980: A numerical investigation of several factors leading to the observed variable intensity of deep convection over South Florida. *J. Appl. Meteor*., **19**, 1037-1063.

van den Heever, S. C. and W. R. Cotton, 2004: The Impact of Hail Size on Simulated Supercell Storms. *J. Atmos. Sci.*, **61,** 1596-1609.

van den Heever, S. C., G. G. Carrio, W. R. Cotton, and P. J. DeMott, 2006: Impacts of nucleating aerosol on Florida storms. Part I: Mesoscale simulations. *J. Atmos. Sci*., **63**, 1752-1775.

Walko, R. L., 1993: Tornado spin-up beneath a convective cell: Required basic structure of the near-field boundary layer winds. *The Tornado: Its Structure, Dynamics, Prediction, and Hazards, Geophys. Monogr.,* **79**, Amer. Geophys. Union, 89–95.

Weisman, M. L., and H. W. Bluestein, 1985: Dynamics of numerically simulated LP storms. *Preprints, 14th Conf. On Severe Local Storms*, Indianapolis, IN, Amer. Meteor. Soc., 267-270.

Weisman, M. L., and J. B. Klemp, 1982: The dependence of numerically simulated convective storms on vertical wind shear and buoyancy. *Mon. Wea. Rev.,* **110,** 504–520.

Wicker, L. J., and R. B. Wilhelmson, 1995: Simulation and analysis of tornado development and decay within a three-dimensional supercell thunderstorm. *J. Atmos. Sci.,* **52,** 2675–2703.

Wilhelmson, R. B., and J. B. Klemp, 1981: A three-dimensional numerical simulation of splitting severe storms on 3 April 1964. *J. Atmos. Sci.,* **38,** 1581–1600.